

1
2
3
4
5
6
7
8
9
10
11
12
13
14
15
16
17
18
19
20
21
22
23
24
25
26
27
28

In-situ infrared spectroscopy as a non-invasive technique to study carbon sequestration at high pressure and high temperature.

Dr. David Vega-Maza
School of Engineering
Fraser Noble Building (Room 256)
King's College
Aberdeen
AB24 3UE
(Tel direct) +44(0)1224 272672
(Fax general office) +44(0)1224 272497
(Email) d.vega-maza@abdn.ac.uk

29 *In-situ* infrared spectroscopy as a non-invasive technique to study carbon
30 sequestration at high pressure and high temperature.

31

32 Greg A. Mutch^{1,2}, James A. Anderson^{1,2}, Rebecca Walker¹, Giuseppina Cerrato³, Sara
33 Morandi³, Lorenza Operti³ and David Vega-Maza^{2*}

34 ¹Surface Chemistry and Catalysis Group, Department of Chemistry, University of Aberdeen,
35 Aberdeen, UK, AB24 3UE

36 ²Materials and Chemical Engineering Group, School of Engineering, University of Aberdeen,
37 Aberdeen, UK, AB24 3UE

38 ³Università degli Studi di Torino, Dipartimento di Chimica & NIS Inter-departmental Centre &
39 Consorzio INSTM-UdR, Torino, Italy

40 Tel: +44 1224 272672, Email: d.vega-maza@abdn.ac.uk

41 **Abstract**

42 Storage of carbon dioxide in geological formations involves changes in wettability to the host
43 formation during injection and ultimately the formation of inorganic carbonates through
44 mineral trapping. Sequestration locations will be at high pressure and high temperature,
45 thus providing a challenging environment for *in-situ* study. However, infrared spectroscopy
46 (FTIR) with the use of photons is not limited in temperature or pressure and therefore is
47 applicable to study chemical changes to minerals occurring during carbon sequestration.
48 Through the commission of a high pressure/high temperature *in-situ* FTIR cell and the
49 subsequent spectroscopic following of carbonation reactions in synthesised silicate mineral
50 analogues, we document fundamental chemical changes occurring at the nanoscale during
51 carbon storage. Speciation, coordination of carbonate ions to the surface of silicate mineral
52 analogues and changes in surface hydroxyl coverage are observed and discussed, in the
53 context of CO₂ injection and dissolution/mineralisation reactions of reservoir silicate
54 minerals.

55 **Keywords**

56 Carbon capture and storage

57 *In-situ* infrared spectroscopy

58 Supercritical carbon dioxide

59 Geological carbon sequestration

60 Sandstone reservoir

61 Silicate surface chemistry

62

63 **1. Introduction**

64 Capture and geological storage of carbon dioxide (CCS) is typically envisaged for depleted oil
65 and gas reservoirs or saline aquifers (Bachu, 2008; IPCC, 2013). These subsurface formations
66 are ideally suited as they are below depths of 800 m ensuring the presence of scCO₂, which
67 is advantageous due to efficient pore filling of the high density fluid. Furthermore these
68 locations are widely distributed and have a highly connected large pore volume (Benson and
69 Cole, 2008; Haszeldine, 2006). A large volume of potential storage, successful trapping of
70 hydrocarbons, experience with CO₂ injection for enhanced oil recovery (EOR) and successful
71 monitoring and verification in numerous injection projects gives increased confidence in
72 storage security and safety in these locations (Jenkins et al., 2015) However, careful
73 consideration must be given to the tectonics of the reservoir, hydrodynamics of the
74 formation brine and mineralogical aspects when evaluating a potential geological formation
75 (Bachu, 2000).

76

77 There are four carbon dioxide trapping mechanisms in geological burial sites, different in the
78 physics, times scales, storage capacity and security: stratigraphic trapping from low
79 permeability caprock; solubility trapping at the CO₂/brine interface; residual trapping by
80 capillary forces during plume migration and finally mineral trapping involving the
81 precipitation of solid carbonates (Boot-Handford et al., 2014). *In-situ* mineral carbonation to
82 form solid carbonates offers the ultimately secure storage mechanism. It is of fundamental
83 importance to understand the chemical reactions occurring during mineralisation to discover
84 the ultimate state and the effect it may have on the mobility of the subsequently injected
85 supercritical fluid (Cardoso and Andres, 2014). During injection of CO₂ there will be four
86 chemically distinct regions containing decreasing amounts of CO₂ and increasing amounts of
87 water/formation brine, as distance to the injection well increases. The mutual solubility of
88 CO₂ and water is well known (Spycher et al., 2003). Dry scCO₂ will exist near the injection site
89 (Pruess and Müller, 2009) before the scCO₂ plume containing water (wet scCO₂) is present.
90 At the edge of the plume significant amounts of CO₂ will be dissolved in the formation brine
91 with CO₂ concentration decreasing until brine with minimal amounts of dissolved CO₂ is
92 found (Zhang and Bachu, 2011). It is of importance to study wet scCO₂ as it is known to react
93 extensively with both steel pipelines and silicate minerals, with the theoretical potential to
94 aid in “self-sealing” of fractured caprocks through mineralisation with the water carried by
95 the migrating scCO₂ itself (McGrail et al., 2009). Furthermore given the increased buoyancy
96 and diffusivity relative to brine, wet scCO₂ might dominate the caprock-reservoir interface
97 during injection (Loring et al., 2011).

98

99 Typically the approach to understand carbonation involves *ex-situ* measurements to quantify
100 carbonate conversion over longer time periods, relevant to the slow reaction kinetics of the
101 overall process (Sanna et al., 2014), particularly mineral dissolution. However, carbonate
102 formation on reactive cations located on the surface should occur on much shorter
103 timescales and it is known that changes in surface area due to chemical reaction are critical
104 to understand permeability in storage formations (Bolourinejad et al., 2014; Bourg et al.,
105 2015). *In-situ* spectroscopic techniques provide a tool to follow chemical reactions at the

106 molecular scale, assuming suitable integration with high pressure and high temperature
107 reaction cells.

108

109 *In-situ* infrared spectroscopy has been applied previously to study the interaction of CO₂
110 with alkaline cations at high pressure in clays (Krukowski et al., 2015; Loring et al., 2014,
111 2012a; Schaef et al., 2015), mineral carbonation reactions with silicate minerals (Loring et
112 al., 2012b, 2011; Miller et al., 2013; Murphy et al., 2011, 2010; Thompson et al., 2013) and
113 carbon storage related fluid mixtures (Danten et al., 2005; Foltran et al., 2015; Oparin et al.,
114 2005, 2004; Wang et al., 2013). An example of the design and construction of an automated
115 high-pressure titration system with *in-situ* infrared access and subsequent application to CO₂
116 sorption in clay, carbonation of silicate mineral and determination of water solubility all at
117 50 °C and 90 bar serves as an excellent introduction to this approach (Thompson et al.,
118 2014).

119

120 Here we report the synthesis and characterisation of silicate mineral analogues, by locating a
121 reactive cation on the surface of amorphous silica, to facilitate the study of surface
122 chemistry changes occurring during CO₂ storage and carbonate mineralisation. Although the
123 synthesised material surface is unrealistically reactive as compared to natural subsurface
124 silicate minerals, it provides the opportunity to study carbonate speciation at realistic
125 storage conditions and on a timescale amenable to *in-situ* spectroscopic investigation.
126 Amorphous silica consists of silicon-oxygen tetrahedra (Zhuravlev, 2000) which are a
127 constituent motif in many subsurface solids. For example muscovite, commonly known as
128 mica, consists of two tetrahedral silicate layers and an intermediate octahedral aluminium
129 layer, with surface charge balance achieved by K⁺ (Wan et al., 2014). Clay minerals in general
130 are composed of silica and/or alumina tetrahedra/octahedra, as are chain, sheet and
131 framework silicate minerals. These are of interest for mineralisation when considering the
132 release of reactive cations due to the pH drop associated with CO₂ injection (Yang et al.,
133 2014). Sandstone formations, consisting primarily of quartz, feldspars, dolomite, calcite,
134 siderite and kaolinite contain sources of divalent and monovalent cations available for
135 mineral trapping (De Silva et al., 2015) forming insoluble and soluble carbonates
136 respectively. The release of cations is also associated with enhancing solubility trapping. The
137 dissolution of feldspar is known to aid solubility trapping through increasing the
138 concentration of soluble carbonates and bicarbonates in solution (Xu et al., 2004). The
139 increased concentration of potassium in reservoir brine has been used as an indicator of the
140 dissolution of K-feldspar due to the interaction with CO₂ (Horner et al., 2015; Pauwels et al.,
141 2007). Furthermore the solubility of silicate minerals generally are known to be sensitive to
142 the presence of carbonate ligands and oxalate ligands (Berg and Banwart, 2000; Wigley et
143 al., 2013), highlighting the importance of understanding the formation of both soluble and
144 insoluble carbonates at sequestration conditions.

145

146 In this work traditional surface chemistry techniques were applied to study cation
147 distribution and the formation of surface carbonates *in-vacuo*. Custom-made high
148 pressure/high temperature *in-situ* FTIR apparatus was subsequently used to
149 spectroscopically follow the carbonation reaction at conditions relevant to geological
150 storage of CO₂, particularly those of wet scCO₂ as above. Carbonate formation was

151 confirmed with coordination to the surface elucidated, a fundamental level of detail often
152 included in surface chemistry/catalysis works but less common in the CCS literature.
153 Changes in surface hydroxyl coverage and the influence of these on the interpretation of the
154 carbonation results are discussed.

155

156 **2. Experimental**

157

158 **2.1 Methodology**

159 Identification of chemisorbed carbonate species formed during carbon storage is
160 fundamental for understanding mechanistic details of mineral carbonation. To gain such a
161 level of detail it is necessary to study carbonate formation at the individual ion level at
162 realistic process conditions. Therefore a silicate mineral analogue (K-SiO₂) was prepared that
163 located a reactive cation on the surface of amorphous silica (SiO₂) through an ion-exchange
164 procedure with surface hydroxyl groups. A detailed description of the synthesis procedure
165 can be found in the Supplementary Information. The synthesised material was first
166 characterised with N₂ adsorption/desorption, thermo-gravimetric analysis (TGA), powder X-
167 ray diffraction (XRD) and scanning electron microscopy (SEM) to understand physico-
168 chemical changes occurring during the ion-exchange synthesis and to determine the extent
169 of metal loading. Detail on the apparatus and experimental procedures can be found in the
170 Supplementary Information. A comparison was made between amorphous SiO₂ and
171 potassium doped SiO₂ to ensure successful cation exchange on the blank silica material.
172 Pellets of the potassium doped SiO₂ were first studied under high-vacuum conditions with
173 transmission *in-situ* FTIR capabilities, where control of the surface chemistry and surface
174 cleaning through high temperature pre-treatment was relatively simple. The sample was
175 exposed to minute quantities of CO₂ allowing spectroscopic identification of the initial stages
176 of carbonate formation. Carbonate coordination to the reactive cation was also established.
177 To ensure similarity between K-SiO₂ as prepared and that studied following the high
178 temperature pre-treatment *in-vacuo*, physico-chemical characterisation was conducted on a
179 portion of potassium doped silica calcined at a temperature above that of the pre-treatment
180 condition (K-SiO₂-450). In subsequent experiments potassium doped SiO₂ was exposed to
181 wet scCO₂ at conditions relevant for geological sequestration, with high pressure/high
182 temperature transmission *in-situ* FTIR investigation. As the reaction proceeds rapidly in
183 these conditions due to the highly reactive synthesised surface, automated spectral
184 acquisition was employed. Similarities in carbonate speciation in the two different pressure
185 regimes were investigated. Finally the effect of temperature on the carbonate and water
186 content was explored.

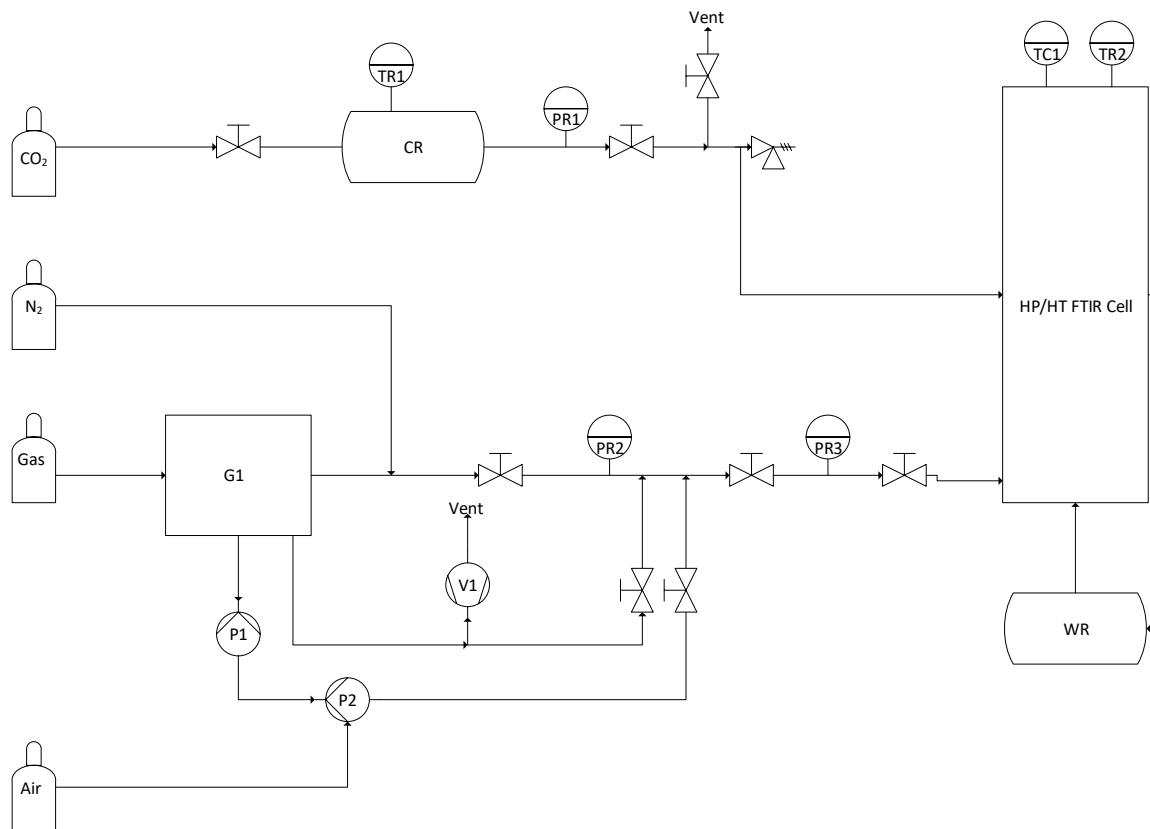
187

188

189 **2.2 High pressure/high temperature *in-situ* FTIR spectroscopy**

190 A high pressure/high temperature FTIR apparatus (Figure 1) was commissioned in-house
191 from a custom Inconel 600 transmission FTIR cell with an internal volume of 23 mL, water-
192 cooled optical grade CaF₂ windows, high performance O-rings (Kalrez®) and gaskets (AgCu),
193 adapted from a previous design (Anderson et al., 1991; Gallei and Schadow, 1974). The
194 internal optical path length of the cell was reduced to <1 mm by inclusion of a CaF₂ spacer.

Instrument List		Equipment List	
Displayed Text	Description	Displayed Text	Description
PR1	RS Components 0 - 25 MPa Pressure Transducer	CR	Liquid CO ₂ Reservoir
PR2	Omega 0 - 25 MPa Pressure Transducer	P1	Maximator DLE 75-50 Pneumatic Gas Booster
PR3	Bourdon Gauge Pressure Transducer	P2	ASF 8050 D Mechanical Pump
TC1	Eurotherm 818 Temperature Controller	V1	Edwards E2M2 Rotary Vane Vacuum Pump
TR1	Omega Class A Pt100 Resistance Temperature Detector	WR	Haake K20 Circulating Water Reservoir
TR2	K-Type Thermocouple	G1	Signal, Series 850 Gas Blender



195

196

Figure 1 - Schematic of high pressure/high temperature in-situ FT-IR spectroscopy apparatus.

197

198

199

200

201

202

203

204

205

206

207

208

209

210

211

212

213

214

Liquid CO₂ (BOC, 99.98%) was first collected in a gas sampling cylinder liquid CO₂ reservoir, followed by expansion through high pressure 316-type stainless steel Swagelok® tubing, fittings and valves into the FTIR cell. Pressure and temperature within the liquid CO₂ reservoir were monitored by a high accuracy pressure transducer (PR1) (Omega®, 0 – 25 MPa, ± 0.05%) and a surface-mounted Class A Pt100 resistance temperature detector RTD (TR1). Temperature and pressure within the FTIR cell were monitored and controlled by a K-type thermocouple (TR2) positioned directly above the sample, a temperature controller (TC1) (Eurotherm Controls, 818), two 500 W, 240 V cartridge heaters and pressure transducer (PR3) (RS Components, 0 – 25 MPa, ±0.25 %), respectively. The cell is operational to 20 MPa and 500 °C and also includes the possibility to control temperature *via* a circulating water bath (Haake K20), evacuate the entire apparatus (V1) (Edwards, E2M2 Rotary Vane Dual Stage) and pressurise gas mixtures through a combination of gas blender (Signal, Series 850), mechanical pump (P2) (ASF, 8050 D) and pneumatic gas booster (P1) (MAXIMATOR, DLE 75-50).

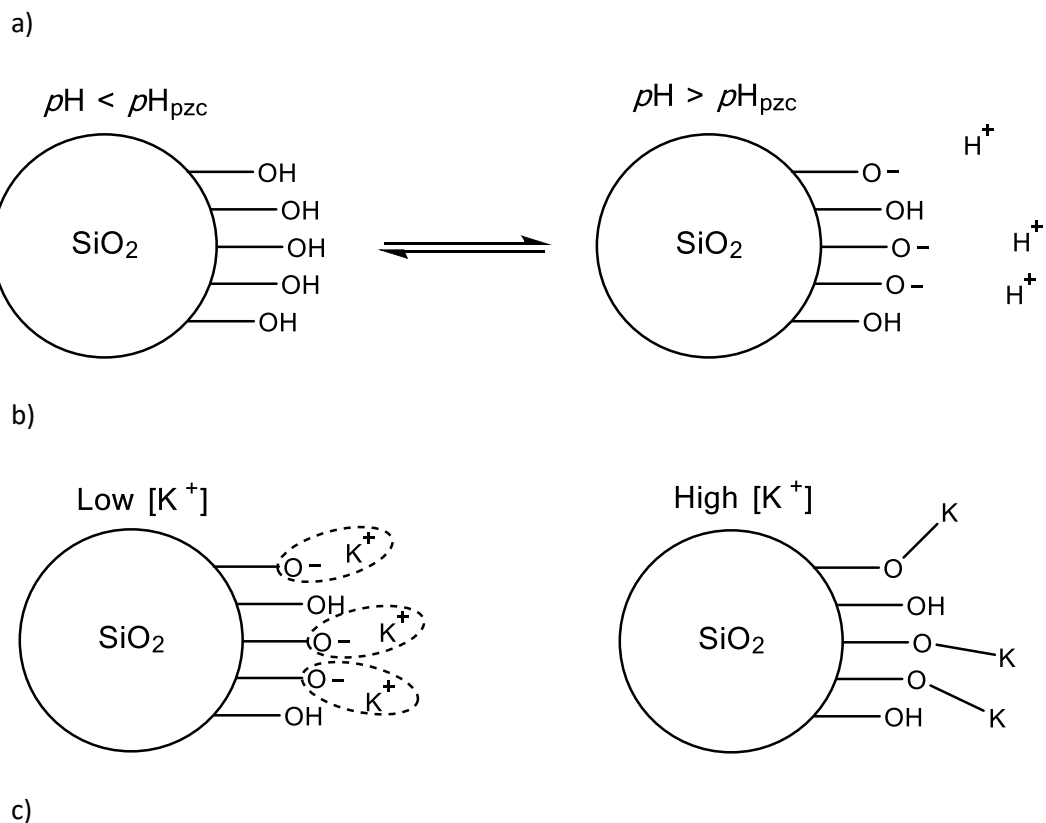
Self-supporting pellets of *ca.* 40 mg of K-SiO₂ were prepared in a 23 mm diameter press at 2 tons (Specac 15.011 Manual Hydraulic Press). Pellets were < 1mm thick and prior to loading in the FTIR cell were cut in half to allow additional discrete monitoring of the fluid phase.

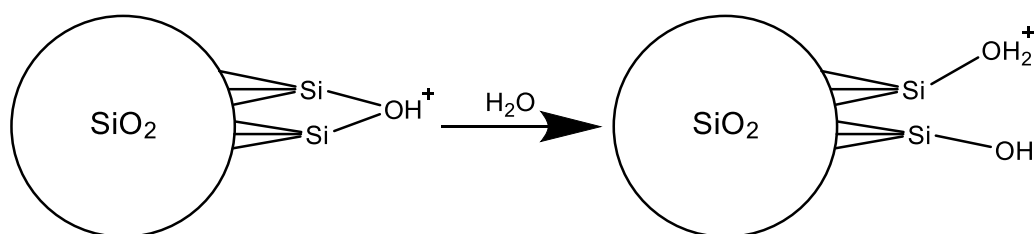
215 Spectra were recorded with an FTIR spectrometer (PerkinElmer Spectrum 100) equipped
 216 with automated collection software (PerkinElmer Timebase) and a liquid nitrogen-cooled
 217 MCT detector. A background spectrum was recorded in the absence of CO₂ and sample, and
 218 was subtracted from all subsequent spectra. At this point, the spectrometer was moved into
 219 position to allow the beam to pass through the transmission window and sample.
 220 Automated spectral acquisition was initiated followed by expansion of CO₂ from the liquid
 221 CO₂ reservoir into the FTIR cell. All spectra including background were recorded at 4 cm⁻¹
 222 resolution with a minimum of 32 accumulated scans per spectrum across a range of 4500 –
 223 500 cm⁻¹. Automated spectral acquisition software was set to record a spectrum every 36
 224 seconds, which were subsequently subtracted from the first recorded spectrum of the
 225 sample disc in air at the experimental temperature.

227 3 Results & Discussion

228 3.2 Synthesis & characterisation of mineral analogues

229 pH was monitored continuously during the ion-exchange synthesis procedure (Figure S1,
 230 Supplementary Information). The first point was the pH of the dopant solution alone (pH
 231 11.7) before a rapid decrease was seen 30 seconds after contact with amorphous silica. As
 232 silica $pH_{pzc} = 4.1$, (Schwarz et al., 1984) immersion in the above solution leads to
 233 deprotonation of surface hydroxyl groups by modification of the equilibrium in Figure 2a.
 234 Such deprotonation allows both non-specific and specific adsorptive interactions with
 235 cations in solution; at low cation concentrations ion pairs are formed (Si-O⁻ : K⁺_(aq)) before full
 236 cation-exchange occurs at higher concentrations to form (Si-OK) as shown in Figure 2b.
 237





243

244 **Figure 2 – (a) – pH dependant protonation-deprotonation equilibrium of silica surface hydroxyl groups. (b) –**
 245 **Partially deprotonated silica surface ion pairing at low cation solution concentration and full cation-exchange**
 246 **at high cation concentration. (c) – Breakdown of silica network due to protonation and subsequent reaction**
 247 **with water.**

248 As the synthesis solution was 1.0 (mol K⁺)·l⁻¹ the specific cation-exchange interactions
 249 dominate and the maximum uptake as determined previously was achieved (Iordan et al.,
 250 1998). A similar dependence on pH is observed for sodium adsorption on silica, with weak
 251 interactions present at low pH and stronger adsorption possible through cation-exchange at
 252 high pH (Smit et al., 1978). After the initial rapid decrease the measurement was stable at
 253 ca. pH 10.9 for the duration of the mixing, indicating that the cation-exchange equilibrium
 254 and saturation population have been achieved, as both concentration and pH conditions as
 255 discussed above had been satisfied.

256

257 Surface area and porosity data is presented in Table 1 with the associated isotherms and
 258 pore distribution plots given in Figure S2, Supplementary Information. There was a clear
 259 drop in both surface area and pore volume after potassium doping and subsequent
 260 treatment at 450 °C. Isotherms conform to IUPAC Type IV classification, with Type H1
 261 hysteresis loops present in all, indicating the presence of mesopores further evidenced in
 262 the pore size distribution plot (Figure S2, Supplementary Information). Excluded for brevity,
 263 the silica surface area after an identical treatment in Ultra-Pure Type I water was 252 m²·g⁻¹
 264 indicating that the decrease in surface area during synthesis was due to phenomena
 265 associated with the cation-exchange procedure and not from physical agglomeration of silica
 266 particles.

267 **Table 1 – Physical characteristics as determined by N₂ adsorption-desorption of fresh and potassium doped**
 268 **silicas as prepared and after treatment at 450 °C in air.**

Sample	Surface Area / m ² ·g ⁻¹	Pore Volume / cm ³ ·g ⁻¹
SiO ₂	257	1.72
K-SiO ₂	69	0.46
K-SiO ₂ -450	51	0.38

269

270 The pore size distribution plots (Figure S2b) indicate that upon cation-exchange there was a
 271 general decrease in pore volume, accompanied by a subtle shift to a lower average pore
 272 width. Considering this fact alongside the high pH synthesis conditions, it is likely that the
 273 pore network has been partially dissolved. At high pH when the surface is negatively charged
 274 due to ionisation (Figure 2a), Si-O bonds are polarised and weakened, enhancing dissolution
 275 and consequently destroying the porous network (Brady and Walther, 1989). It has also
 276 been observed that the presence of cations enhances the rate of silica dissolution (Plettinck
 277 et al., 1994) and that there is a dissolution rate dependence on the particular alkali metal

278 cation, with sodium and potassium hydroxides or chlorides showing the greatest
279 enhancement (Wijnen et al., 1990). At alkaline pH the effect is particularly strong for quartz
280 dissolution in the presence of sodium, 200 times faster than in pure water (Rimstidt, 2015).
281 It is known that protonation of silica increases the Si-O bond distance, in turn weakening the
282 silica network and increasing reactivity with water. This reaction leads to the breaking of the
283 silica network as shown in Figure 2c (Brown et al., 2014). If one substitutes the proton for
284 the adsorption of potassium, it is reasonable to assume at least a similar effect.

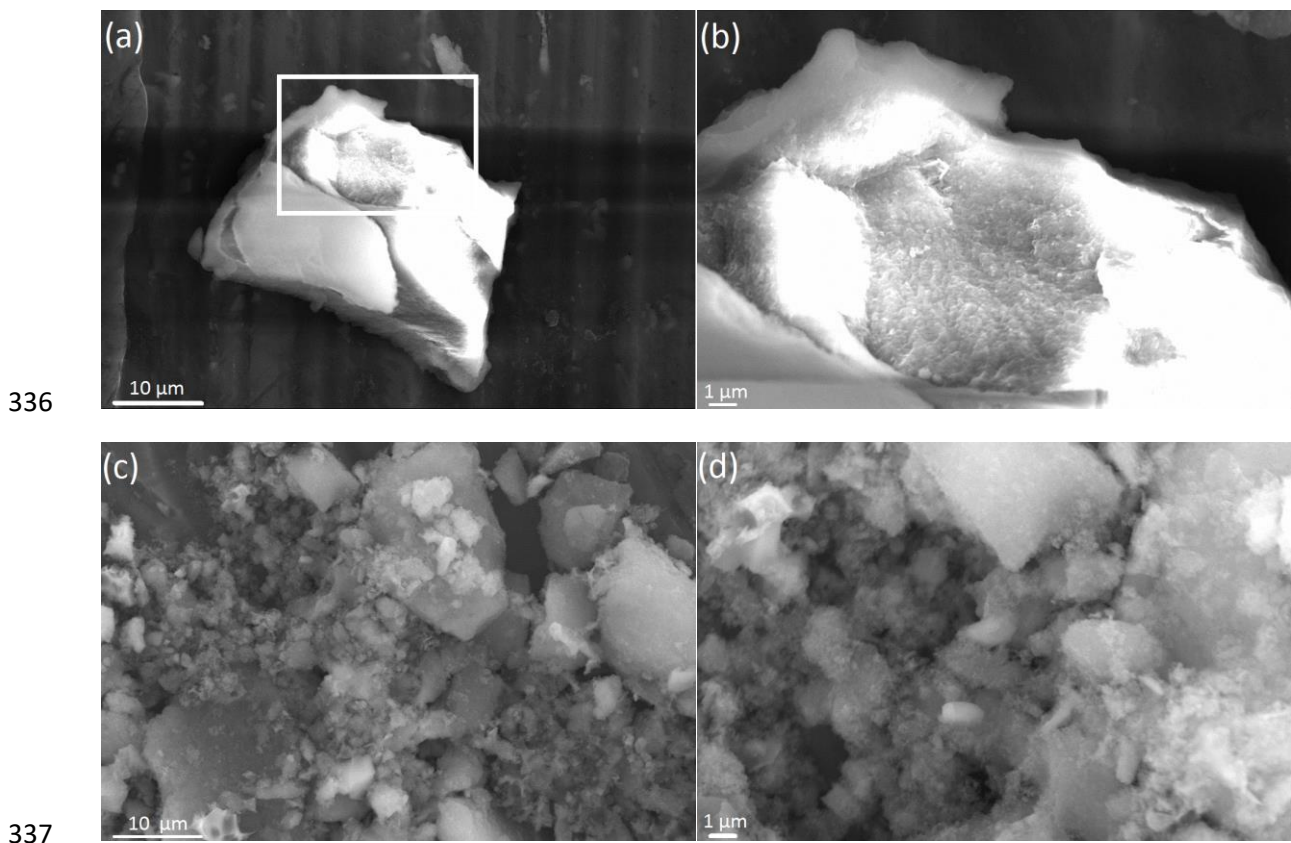
285
286 An alternative scenario to explain this observation would be pore-blockage by the formation
287 of a secondary oxide or hydroxide phase on the silica surface. Without evidence of the
288 formation of a crystalline phase in X-ray diffractograms (Figure S3, Supplementary
289 Information) this seems unlikely. However a disordered non-crystalline secondary phase
290 would occupy a greater volume than the ordered crystalline equivalent which could explain
291 the loss in porosity and surface area and thus cannot be ruled out entirely. A further smaller
292 decrease in surface area and pore volume was apparent after treatment in air at 450 °C,
293 which was possibly due to the onset of cristobalite or tridymite formation, enhanced at
294 lower temperature in the presence of potassium (Iordan et al., 1998). Alternatively this
295 could be due to the formation of crystalline potassium carbonate on the surface. The
296 observation that the pore volume at around 500 Å was largely maintained at the expense of
297 that at 200 Å during this transition would support the idea of formation of cristobalite or
298 tridymite, as the initial loss of the smallest and consequently most unstable pores would be
299 expected during crystallisation.

300
301 X-ray diffractograms are shown in Figure S3, Supplementary Information for both parent and
302 potassium-doped silicas. The broad peak between 16 and 28° 2θ is indicative of amorphous
303 silica and shows that after cation-exchange this amorphous nature is retained. Additional
304 peaks at 30.1 and 31.2° 2θ were observed in the K-SiO₂-450 pattern but are not assignable to
305 either K₂CO₃, quartz or cristobalite. They could be explained by a crystalline silica species e.g.
306 tridymite (ICDD 42-1401) but as intensity of the signal was so low, it is likely arising from a
307 very small amount of poorly crystalline material diluted in a large amount of amorphous
308 silica. A conclusive identification was not possible and assertion of a positive identification
309 would be misleading.

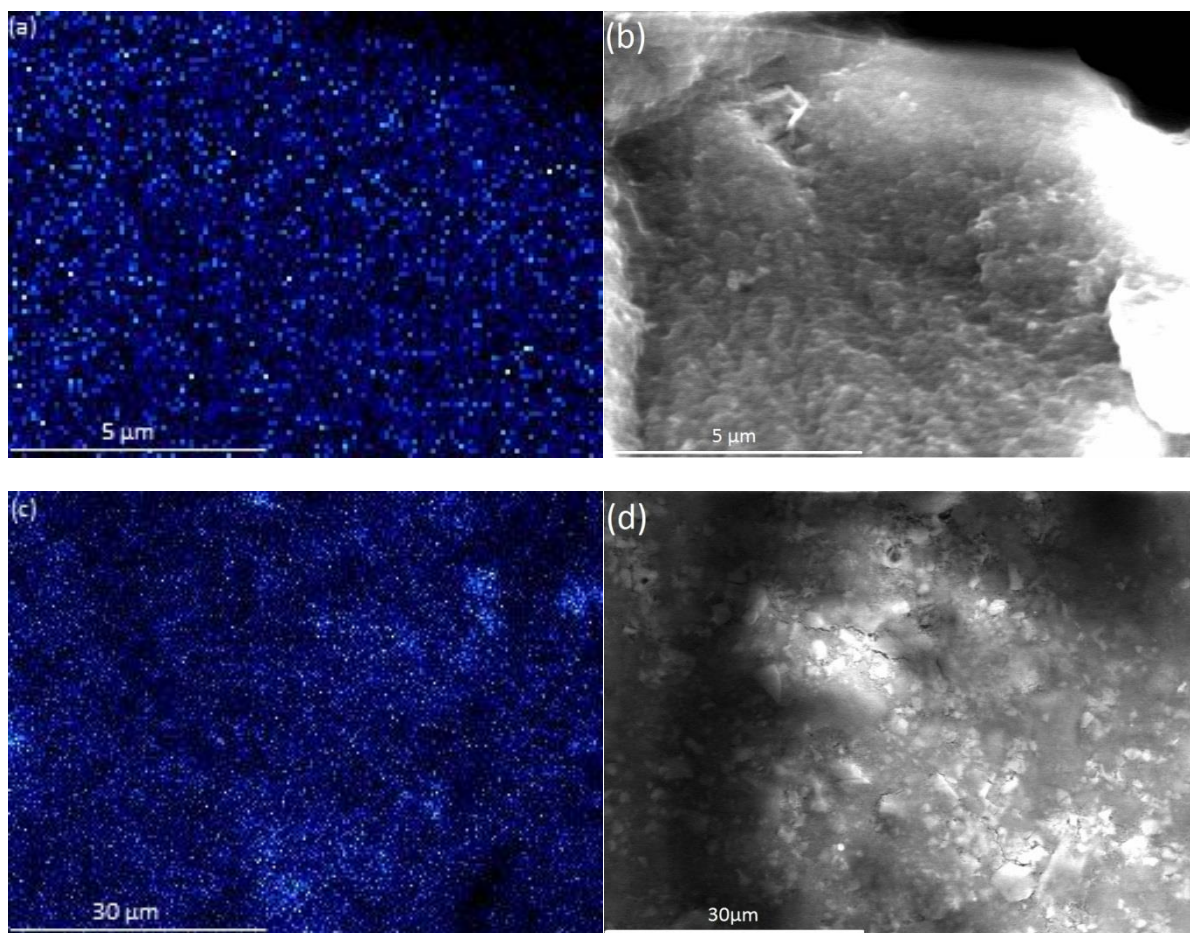
310
311 SEM images of K-SiO₂ (Figures 3a and b) and K-SiO₂-450 (Figures 3c and d) indicated the
312 presence of amorphous silica aggregates throughout ranging from <1 to 30 μm, in
313 agreement with the amorphous nature determined by XRD. EDX elemental maps of
314 potassium within K-SiO₂ (Figure 4a) and K-SiO₂-450 (Figure 4c) collected from regions shown
315 in Figure 4b and Figure 4d, respectively, showed that potassium was generally well dispersed
316 within the sample, at different length scales, as-prepared and after treatment at high
317 temperature. The cation loading appeared to be consistent across the surface, without the
318 formation of concentrated regions of potassium indicative of a segregated secondary phase,
319 consistent with the lack of K₂CO₃ observed in XRD. The results of the semi-quantitative EDX
320 analysis (Table 2) indicated that potassium doping was significant with a level of 6.93 ± 0.03
321 wt% reached during synthesis and maintained after heat treatment. This was in excellent

322 agreement with the original publication which determined a loading of 6.9 wt% K⁺ using a
323 1.01 (mol K⁺)·l⁻¹ solution of K₂CO₃ (Iordan et al., 1998).

324
325 Considering the Kiselev-Zhuravlev value of 4.6 (least-squares) or 4.9 OH·nm⁻² (arithmetical
326 mean), which gives the number of hydroxyl groups per unit surface area when the degree of
327 hydroxylation is at a maximum, one can determine a surface coverage of potassium by also
328 using the surface area and potassium loading determined by EDX (Zhuravlev, 2000). Using
329 the surface area of the water treated sample (252 m²·g⁻¹) a surface coverage of 92.1 or
330 86.4% was determined by using the least-squares and arithmetical mean respectively. Detail
331 of the calculation is given in the Supplementary Information. It is important to consider the
332 limitations of a model that uses maximum hydroxylation when the cation-exchange
333 procedure relies on extensive dihydroxylation. However, as the silica used for synthesis was
334 not dried or heat treated before exposure to the dopant solution, the conclusions
335 surrounding coverage are valid.



338 **Figure 3 – SEM images of K-SiO₂ at (a) 5000x and (b) framed section in (a) at 15000x magnification as prepared**
339 **and at (c) 5000x and (d) 15000x magnification after treatment at 450 °C in air. Aggregates of amorphous silica**
340 **are visible in all images.**



341

342

343

344

345

346

Figure 4 – (a) EDX map of potassium dispersion within K-SiO₂ as prepared, (b) site for map (a) of powder K-SiO₂ at 30000x magnification, (c) EDX map of potassium dispersion with K-SiO₂-450, (d) site for map (c) of pelletised K-SiO₂ at 5000x magnification. Potassium is well dispersed throughout the samples, before and after heat treatment and at both length scales.

347

348

Table 2 – Data obtained from EDX analysis of fresh and potassium doped silicas as prepared and after treatment at 450 °C in air. Values reported with standard deviation on average of multiple points.

Sample	Si / wt%	O / wt%	K ⁺ / wt%
SiO ₂	43.99 ± 0.45	56.01 ± 0.45	
K-SiO ₂	39.01 ± 0.28	54.06 ± 0.32	6.93 ± 0.03
K-SiO ₂ -450	36.79 ± 0.12	53.82 ± 0.16	7.41 ± 0.04

349

350

351

352

353

354

355

356

357

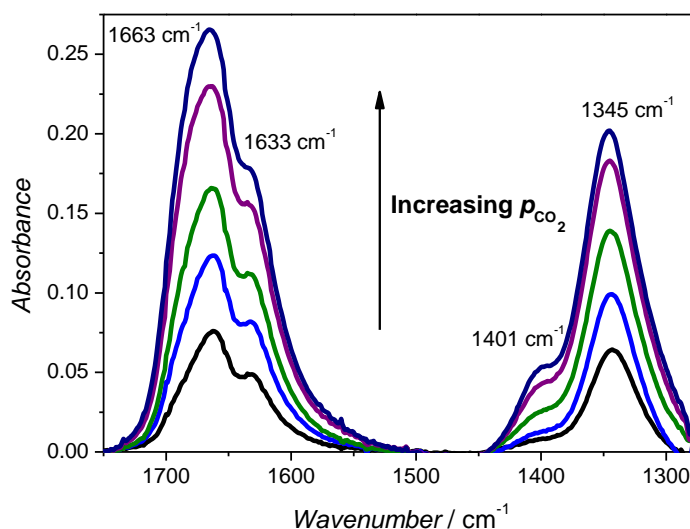
358

359

360

Carbon dioxide is routinely used in surface chemistry studies to probe the nature of Lewis acid sites through electronic σ -donation *via* the oxygen lone-pair or Lewis base sites through reactive adsorption to form carbonate, bicarbonate or formate species, respectively (Busca and Lorenzelli, 1982). Characteristic absorption bands are used to differentiate surface complexes. Therefore regarding the *in-vacuo* FTIR investigation, the formation of surface carbonates (as opposed to bulk carbonates) on K-SiO₂ surface was evidenced (Figure 5) by growth of bands due to vibrations in the range 1750 – 1275 cm⁻¹ as a function of CO₂ pressure. This was an initial indication that the loading of potassium had been successful and implied that it was located on the surface, consistent with the sub-monolayer coverage calculations above. Based on changes in intensity during outgassing (not shown for brevity), peaks at 1633/1345 cm⁻¹ and 1663/1401 cm⁻¹ were assigned as associated pairs. Upon

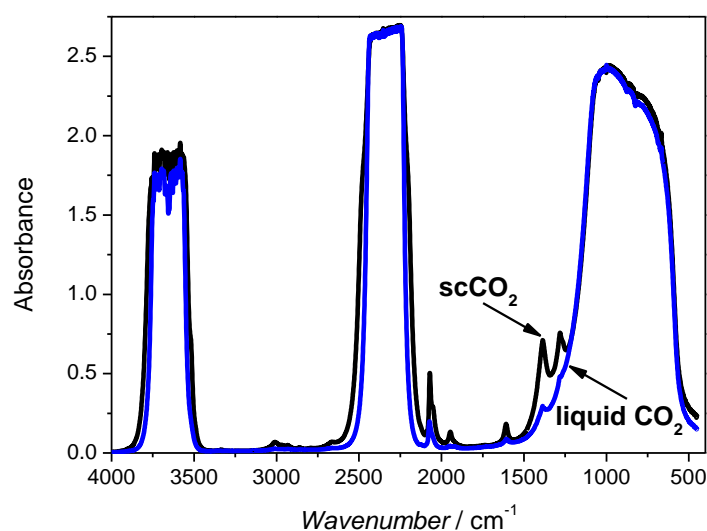
361 coordination to a surface, carbonate ion symmetry is lowered and consequently the
 362 degenerate ν_3 asymmetric carbon-oxygen stretch at 1415 cm^{-1} is split into pairs. As first
 363 proposed by (Nakamoto et al., 1957), the magnitude of the splitting indicates whether the
 364 surface species is ionic ($< 50\text{ cm}^{-1}$), monodentate (100 cm^{-1}), bidentate (300 cm^{-1}) or bridged
 365 ($\geq 400\text{ cm}^{-1}$). The bands in Figure 5 had a $\Delta\nu_3$ of *ca.* 288 and 262 cm^{-1} , respectively which
 366 implied a bidentate coordination to the potassium cation.



367
 368 **Figure 5 – Evolution of bands assigned to bidentate carbonates on K-SiO₂ at 1750 – 1275 cm⁻¹ as a function of**
 369 **CO₂ pressure from 0.025 – 20.8 mbar. Spectra were recorded at room temperature and are plotted as**
 370 **difference spectra relative to K-SiO₂ after treatment *in-vacuo* at 400 °C.**

371 **3.3 High pressure *in-situ* FTIR spectroscopy**

372 Figure 6 shows typical FTIR spectra of CO₂ at conditions relevant to this work, in both the
 373 liquid and supercritical state. Broad bands at *ca.* 3700 cm^{-1} and 2350 cm^{-1} were assigned to a
 374 band due to a combination mode ($\nu_1 + \nu_3$) and the asymmetric stretch respectively. The
 375 narrow band around 2075 cm^{-1} was attributable to a combination of symmetric bend and
 376 symmetric stretch. Weak bands visible in the liquid CO₂ spectrum included a band due to a
 377 combination mode at 3012 cm^{-1} from the symmetric bend and asymmetric stretch, a band at
 378 1949 cm^{-1} from symmetric bend and symmetric stretch combination and a peak at 1610 cm^{-1}
 379 attributed to the OH bending vibration of water. Bands at 1388 and 1282 cm^{-1} which are
 380 enhanced by Fermi resonance were suppressed during the transition from liquid to
 381 supercritical CO₂. These served as a good example of the general loss in intensity of many of
 382 the bands observed during this transition, with the most intense broad bands at 3700 and
 383 2350 cm^{-1} narrowing also. Two bending modes of CO₂ at 666 cm^{-1} were not visible due to the
 384 cut-off of the optical windows. Band assignments for CO₂ are given in (Yagi et al., 1993) and
 385 for carbonates from (Busca and Lorenzelli, 1982)



386

387
388
389

Figure 6 – FT-IR spectra of liquid carbon dioxide (black) at 19 °C and supercritical carbon dioxide (blue) at 50 °C after isochoric heating. The intensities of most of the vibrational bands decrease upon transition from liquid to supercritical phase, or in the case of the most intense bands, narrow slightly.

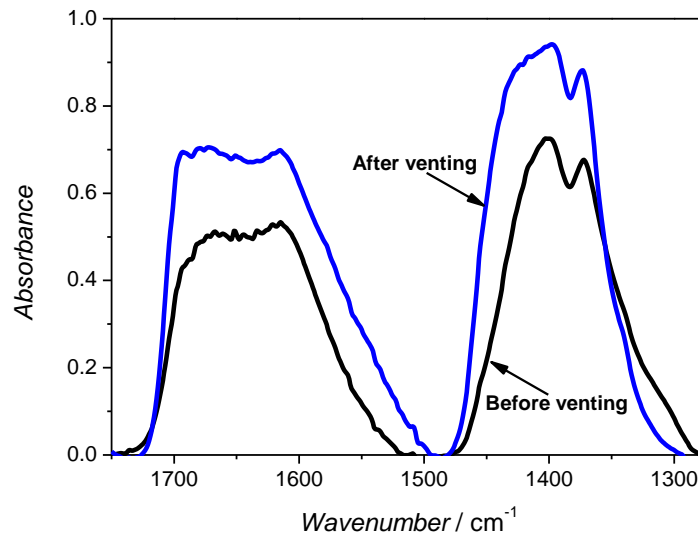
390
391
392
393
394
395
396
397
398
399
400
401
402
403
404
405
406
407
408

Immediately upon immersion in scCO₂ at 50 °C and 4.92 MPa, K-SiO₂ formed bidentate carbonates (Figure 7) comparable with those formed *in-vacuo* (Figure 5). Plotted as difference spectra relative to K-SiO₂ at 50 °C in air before expansion of liquid CO₂ into the cell, the black (before venting) spectrum was recorded 10 minutes after expansion into the cell. The blue spectrum (after venting) was recorded following 48 h immersion under the conditions above and subsequent venting of the scCO₂, indicating that the formed carbonates remained stable in the absence of the fluid phase scCO₂. In order to investigate the evolution of the carbonate bands, automatic acquisition software was employed to record spectra immediately following expansion into the high pressure cell. It was observed (Figure 8) that at 50 °C and 5.29 MPa the development of bidentate carbonate was rapid with bands at 1750 – 1300 cm⁻¹ showing uniform growth against time. In both sets of spectra (Figure 7 and Figure 8) it was observed that $\Delta\nu_3$ was consistent with the results *in-vacuo* and thus it was assumed that the relationships between pairs of degenerate bands were unchanged. If a position of 1680 cm⁻¹ is taken for the highest frequency band (Figure 7 and Figure 8), $\Delta\nu_3$ value for the 1615/1372 cm⁻¹ band pair in (Figure 7) was 243 cm⁻¹ and the 1680/1403 cm⁻¹ band pair was 277 cm⁻¹. In Figure 8 the $\Delta\nu_3$ value for the 1601/1373 cm⁻¹ band pair was 228 cm⁻¹ and the 1680/1417 cm⁻¹ band pair was 263 cm⁻¹. Thus in both the low pressure and high pressure regimes, the species formed upon exposure to scCO₂ are bidentate carbonates for K-SiO₂.

409
410
411
412
413
414
415

These findings are comparable with those of (Loring et al., 2011) who studied the carbonation of forsterite (Mg₂SiO₄) in scCO₂ at 50 °C and 180 atm, evidencing the growth of a magnesium carbonate precipitate through an increase in ν_3 C-O stretching modes at 1480 and 1425 cm⁻¹. A similar conclusion was drawn in the case of the inosilicate mineral wollastonite (CaSiO₃) where features due to carbonate at 1410 cm⁻¹ with a broad shoulder at 1460 cm⁻¹ indicated the formation of potentially hydrated metastable amorphous calcium carbonate phase (Miller et al., 2013). The shoulder appeared to decrease with increasing

416 water saturation of the scCO₂ phase, indicating a change in the speciation of the surface
417 carbonate. It is pertinent to highlight in these two former studies bulk carbonate formation
418 was evidenced, whereas in the current study we show surface carbonate formation. The
419 importance of water was also highlighted, by a lack of reaction in anhydrous scCO₂ (Miller et
420 al., 2013). This issue is overcome in the present study by both trace amounts of water in the
421 liquid CO₂ and those remaining post-synthesis. Zhuravlev defined the removal of physisorbed
422 water from amorphous silica as being complete at 190±10 °C, with subsequent weight loss
423 due to the removal of surface hydroxyl groups (Zhuravlev, 1993, 1989). From the TGA
424 measurements (Figure S4, Supplementary Information), the water content of K-SiO₂ was
425 established as 3.57% (Table S1, Supplementary Information), by taking the numerical
426 average of weight loss at 190±10 °C for the triplicate measurements. scCO₂ is highly efficient
427 at extracting water from amorphous silica (Tripp and Combes, 1998) and therefore the water
428 content of the silica is critical in determining the water content of fluid phase, and as above,
429 the applicability to various stages of CO₂ injection. Considering the ca. 20 mg discs used in
430 the HP/HT *in-situ* FTIR experiments and the quantity of scCO₂ present determined from the
431 volume and experimental thermodynamic conditions (Span and Wagner, 1996), the amount
432 of water present in the scCO₂ was calculated and confirmed we are operating in a wet CO₂
433 regime. Detail of the calculation is given in the Supplementary Information. Furthermore the
434 supercritical line for water-CO₂ mixtures is severely depressed in terms of pressure as
435 compared to pure CO₂ (Jager et al., 2013). Considering the pressures reported for the HP/HT
436 *in-situ* FTIR experiments and that the quantity of water present can only be increased by
437 trace (<20 ppm v/v) water present in the liquid CO₂ as purchased, this is further evidence
438 that we are operating within a wet CO₂ regime. Greater detail on the importance of the
439 presence of water on carbonation reactions is found in (Thompson et al., 2013) where the
440 bicarbonate anion present in the thin water film on the surface of silicate minerals is shown
441 by *in-situ* FTIR. This is a key reaction intermediate, highlighting the advantages of FTIR in
442 elucidating reaction mechanism in wet CO₂ (Thompson et al., 2013).



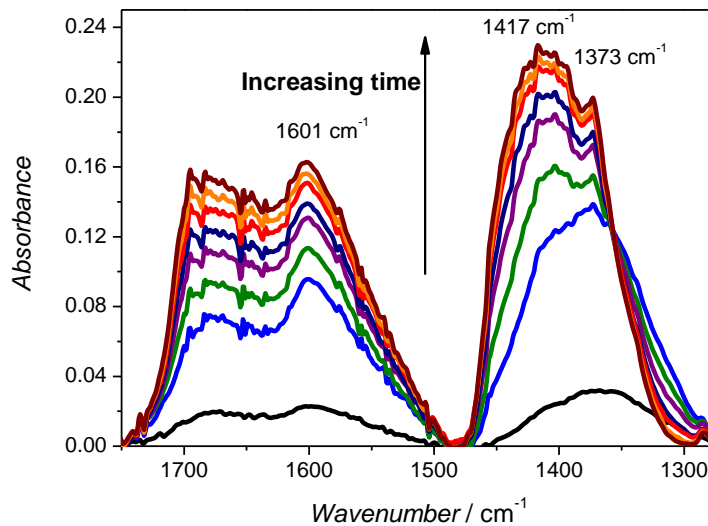
443

444

445

446

Figure 7 – Bands due to bidentate carbonate at 1750 – 1275 cm^{-1} following scCO_2 exposure at 50°C and 4.92 MPa (black) and after venting of scCO_2 following 48 hours immersion under above conditions (blue), plotted as difference spectra relative to K-SiO_2 at 50 °C in air.



447

448

449

450

451

Figure 8 – Evolution of bands due to bidentate carbonate at 1750 – 1275 cm^{-1} during the first 5 minutes of reaction upon scCO_2 exposure at 50°C and 5.29 MPa. The temporal acquisition software recorded each spectrum at an interval of 36 seconds and spectra are plotted as difference spectra relative to K-SiO_2 at 50 °C in air.

452

453

454

455

456

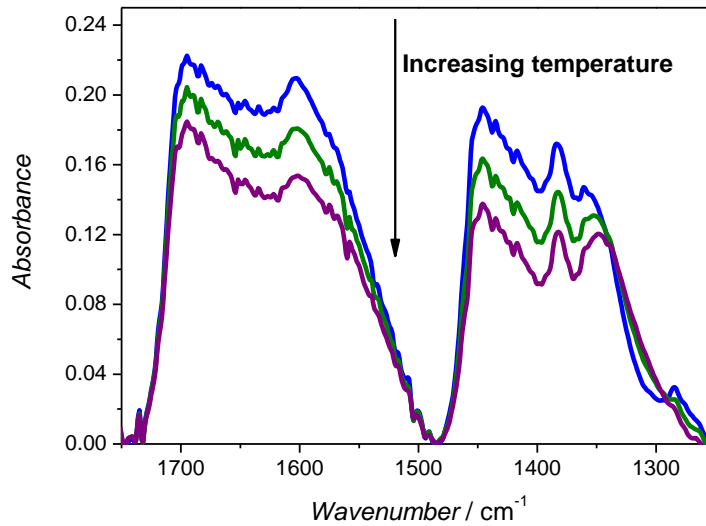
457

458

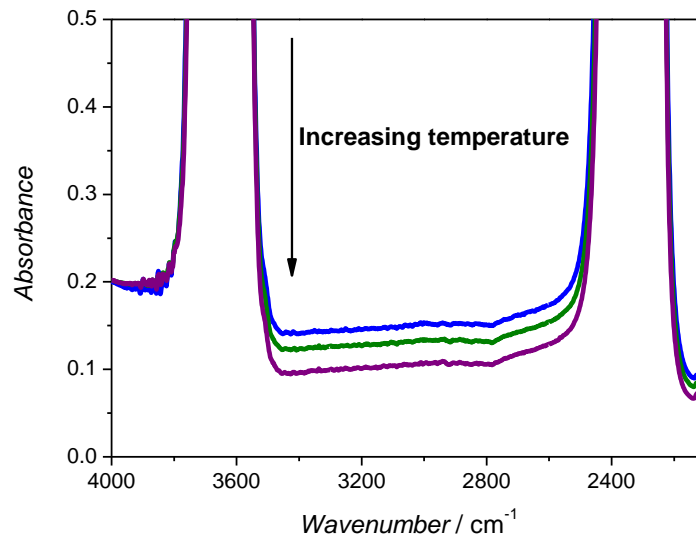
As carbon storage is envisaged for geological formations, the influence of depth (and thus temperature) is important. It has been shown (Hur et al., 2013) that cation type and the presence of water is important in determining carbonate formation as above. It was also shown that upon moving from liquid to supercritical CO_2 the carbonate formation reaction at the internal surfaces became possible due to the lower viscosity and higher diffusivity achieved in the supercritical regime. Carbonates formed on calcium exchanged montmorillonite but not in sodium exchanged clay, with the speciation of carbonates as

459 determined by FTIR changing depending on the phase of CO₂ present. Thus the influence of
460 temperature on the carbonation of K-SiO₂ was investigated (Figure 9a) at 50 °C and 5.84 MPa
461 (blue), 70 °C and 5.98 MPa (green) and 90 °C and 6.09 MPa (purple). Due to the design of the
462 cell, both temperature and pressure are inherently linked and therefore discrimination of
463 the effect of each parameter was not possible. Initially it appeared that the magnitude of
464 carbonation decreased with increasing temperature (Figure 9a), but upon investigation
465 across the spectral region attributable to surface hydroxyl groups (Figure 9b), it can be seen
466 that in fact the sample was being dried, due to a combination of increased temperature and
467 the well-known drying effect of scCO₂ (Kim et al., 2012; Tripp and Combes, 1998). Upon
468 removal of water from K-SiO₂, the transmission properties of the sample improved and thus
469 the apparent absorption across the whole spectrum decreased, leading to the false
470 assumption that the carbonate population was decreasing.

471 It is interesting to note that there is no change in the carbonate coordination to the surface
472 as it has been shown previously in forsterite that water concentration directly impacted
473 carbonate coordination (Loring et al., 2015). Below a threshold value of 76 (μmol H₂O)·m⁻²
474 carbonate complexes were formed, with bidentate coordination observed at the lowest
475 water concentrations. Considering the current results where bidentate coordination was
476 observed throughout the experiment, this would imply that we began with a minimal
477 amount of adsorbed water (< 76 (μmol H₂O)·m⁻²) and subsequent drying thus had no impact
478 on the coordination of the adsorbed carbonate species. Considering the water content
479 determined by TGA, the surface area of K-SiO₂ and the average pellet mass, the adsorbed
480 water present before experiment was 29 (μmol H₂O)·m⁻², in excellent agreement with the
481 spectroscopic findings. Detail of the calculation is given in the Supplementary Information.
482 Generally, considering the small changes in absorption, it is likely that the magnitude of
483 carbonation was unaffected by the small change in temperature. However it is important to
484 comment on the changes observed in the hydroxyl group region, as it is known that
485 wettability directly influences plume migration and residual trapping (Bourg et al., 2015). It is
486 accepted that changes to the hydrophilicity, particularly at the pore scale, have significant
487 impact on wettability and thus geological storage of CO₂ (Chen et al., 2015) and these results
488 suggested that to study them at high pressure and high temperature, *in-situ* FTIR may be a
489 suitable tool. Indeed inaccessible hydroxyl groups on silica are accessible in scCO₂ (McCool
490 and Tripp, 2005) and therefore CO₂ is regarded as being highly effective at removing water
491 from silica (Dickson et al., 2006), consistent with our observations.



492



493

494 Figure 9 – (a) Changes in carbonate band intensity (1750 – 1275 cm^{-1}) at 50 °C and 5.84 MPa (blue), 70 °C and
 495 5.98 MPa (green) and 90 °C and 6.09 MPa (purple). (b) Changes in OH region during same experiment showing
 496 drying of K-SiO₂ with increased temperature and pressure, 50 °C and 5.84 MPa (blue), 70 °C and 5.98 MPa
 497 (green) and 90 °C and 6.09 MPa (purple).

498 **4 Conclusions**

499 In this paper, it was shown that through the preparation of cation-doped silica, one can
 500 produce a model system that facilitates fundamental understanding associated with
 501 chemical changes to host mineralogy during carbon sequestration. An investigation of
 502 surface chemistry changes occurring during exposure to sCO₂ has been performed in a
 503 custom high pressure/high temperature FTIR cell and was shown to be comparable with
 504 more conventional surface chemistry high vacuum FTIR methods. The carbonation of
 505 potassium doped silica, as a simple model system for the surface of silicate minerals, was
 506 possible in pressure and temperature conditions relevant to geological sequestration of
 507 carbon dioxide, with potential implications for mineral dissolution. In all cases the

508 carbonation reaction produced bidentate carbonates on the surface of potassium doped
509 silica indicating sufficient reactivity for the mineralisation of scCO₂. As the surface of a
510 mineral or the interfacial region between scCO₂ and mineral will be the initial point of
511 contact during EOR or CCS, it is of fundamental importance to understand the nature of
512 reaction products. Furthermore the nature of the ligand is known to influence the
513 dissolution rate of minerals during CCS and therefore obtaining carbonate speciation/cation
514 coordination is of importance. Further work is ongoing to determine the role of cation and
515 the presence of water on the speciation of formed carbonates. In general it has been shown
516 that FTIR can be used to understand EOR and CCS processes in challenging environments.

517 **Acknowledgements**

518 We would like to thank EPSRC for a Doctoral Training Grant (G.A.M) and the Erasmus
519 programme for supporting the study visit to Turin (R.W). We would also like to thank Dr.
520 Federico Cesano for SEM/EDX measurements and for fruitful discussion. Dr. Jo Duncan is
521 thanked for his tremendous insight during XRD interpretation.

522 **References**

- 523 Anderson, J.A., McQuire, M.W., Rochester, C.H., Sweeney, T., 1991. In situ FTIR study of CO/H₂
524 reactions over Rh/SiO₂ catalysts at high pressure and temperature. *Catal. Today* 9, 23–30.
525 doi:10.1016/0920-5861(91)85003-Q
- 526 Bachu, S., 2008. CO₂ storage in geological media: Role, means, status and barriers to deployment.
527 *Prog. Energy Combust. Sci.* 34, 254–273. doi:10.1016/j.pecs.2007.10.001
- 528 Bachu, S., 2000. Sequestration of CO₂ in geological media: Criteria and approach for site selection in
529 response to climate change. *Energy Convers. Manag.* 41, 953–970. doi:10.1016/S0196-
530 8904(99)00149-1
- 531 Benson, S.M., Cole, D.R., 2008. CO₂ Sequestration in Deep Sedimentary Formations. *Elements* 4,
532 325–331. doi:10.2113/gselements.4.5.325
- 533 Berg, A., Banwart, S. a., 2000. Carbon dioxide mediated dissolution of Ca-feldspar: Implications for
534 silicate weathering. *Chem. Geol.* 163, 25–42. doi:10.1016/S0009-2541(99)00132-1
- 535 Bolourinejad, P., Shoeibi Omrani, P., Herber, R., 2014. Effect of reactive surface area of minerals on
536 mineralization and carbon dioxide trapping in a depleted gas reservoir. *Int. J. Greenh. Gas*
537 *Control* 21, 11–22. doi:10.1016/j.ijggc.2013.11.020
- 538 Boot-Handford, M.E., Abanades, J.C., Anthony, E.J., Blunt, M.J., Brandani, S., Mac Dowell, N.,
539 Fernández, J.R., Ferrari, M.-C., Gross, R., Hallett, J.P., Haszeldine, R.S., Heptonstall, P., Lyngfelt,
540 A., Makuch, Z., Mangano, E., Porter, R.T.J., Pourkashanian, M., Rochelle, G.T., Shah, N., Yao,
541 J.G., Fennell, P.S., 2014. Carbon capture and storage update. *Energy Environ. Sci.* 7, 130.
542 doi:10.1039/c3ee42350f
- 543 Bourg, I., Beekingham, L., DePaolo, D.J., 2015. The Nanoscale Basis of CO₂ Trapping for Geologic
544 Storage. *Environ. Sci. Technol.* 49, 10265–10284. doi:10.1021/acs.est.5b03003

- 545 Brady, P. V., Walther, J. V., 1989. Controls on silicate dissolution rates in neutral and basic pH
546 solutions at 25°C. *Geochim. Cosmochim. Acta* 53, 2823–2830. doi:10.1016/0016-
547 7037(89)90160-9
- 548 Brown, M.A., Arrigoni, M., Heroguel, F., Redondo, A.B., Giordano, L., Bokhoven, J.A. Van, Pacchioni,
549 G., 2014. pH Dependent Electronic and Geometric Structures at the Water – Silica Nanoparticle
550 Interface. *J. Phys. Chem. C* 118, 29007–29016. doi:dx.doi.org/10.1021/jp502262f
- 551 Busca, G., Lorenzelli, V., 1982. Infrared spectroscopic identification of species arising from reactive
552 adsorption of carbon oxides on metal oxide surfaces. *Mater. Chem.* 7, 89–126.
553 doi:10.1016/0390-6035(82)90059-1
- 554 Cardoso, S.S.S., Andres, J.T.H., 2014. Geochemistry of silicate-rich rocks can curtail spreading of
555 carbon dioxide in subsurface aquifers. *Nat. Commun.* 5, 5743. doi:10.1038/ncomms6743
- 556 Chen, C., Zhang, N., Li, W., Song, Y., 2015. Water Contact Angle Dependence with Hydroxyl
557 Functional Groups on Silica Surfaces under CO₂ Sequestration Conditions. *Environ. Sci. Technol.*
558 49, 14680–14687. doi:10.1021/acs.est.5b03646
- 559 Danten, Y., Tassaing, T., Besnard, M., 2005. Infrared and molecular-dynamics studies of the
560 rotational dynamics of water highly diluted in supercritical CO₂. *J. Chem. Phys.* 123, 074505.
561 doi:10.1063/1.1953561
- 562 De Silva, G.P.D., Ranjith, P.G., Perera, M.S. a., 2015. Geochemical aspects of CO₂ sequestration in
563 deep saline aquifers: A review. *Fuel* 155, 128–143. doi:10.1016/j.fuel.2015.03.045
- 564 Dickson, J.L., Gupta, G., Horozov, T.S., Binks, B.P., Johnston, K.P., 2006. Wetting phenomena at the
565 CO₂/water/glass interface. *Langmuir* 22, 2161–2170. doi:10.1021/la0527238
- 566 Foltran, S., Vosper, M.E., Suleiman, N.B., Wriglesworth, A., Ke, J., Drage, T.C., Poliakoff, M., George,
567 M.W., 2015. Understanding the solubility of water in carbon capture and storage mixtures: An
568 FTIR spectroscopic study of H₂O+CO₂+N₂ ternary mixtures. *Int. J. Greenh. Gas Control* 35, 131–
569 137. doi:10.1016/j.ijggc.2015.02.002
- 570 Gallei, E., Schadow, E., 1974. Ultrahigh-vacuum, high pressure and temperature infrared-ultraviolet-
571 visible spectrophotometer cell. *Rev. Sci. Instrum.* 45, 1504 – 1506. doi:10.1063/1.1686547
- 572 Haszeldine, R.S., 2006. Deep Geological CO₂ Storage: Principles Reviewed, and Prospecting for Bio-
573 energy Disposal Sites. *Mitig. Adapt. Strateg. Glob. Chang.* 11, 369–393. doi:10.1007/s11027-
574 005-9005-6
- 575 Horner, K.N., Schacht, U., Haese, R.R., 2015. Characterizing long-term CO₂-water-rock reaction
576 pathways to identify tracers of CO₂ migration during geological storage in a low-salinity,
577 siliciclastic reservoir system. *Chem. Geol.* 399, 123–133. doi:10.1016/j.chemgeo.2014.09.021
- 578 Hur, T.-B., Baltrus, J.P., Howard, B.H., Harbert, W.P., Romanov, V.N., 2013. Carbonate formation in
579 Wyoming montmorillonite under high pressure carbon dioxide. *Int. J. Greenh. Gas Control* 13,
580 149–155. doi:10.1016/j.ijggc.2012.12.001
- 581 Jordan, A., Kappenstein, C., Colmay, E., Zaki, M.I., 1998. Surface contribution to the interfacial
582 chemistry of potassium modified oxide catalysts. *J. Chem. Soc. Faraday Trans.* 94, 1149–1156.

- 583 IPCC, 2013. Working Group I Contribution to the IPCC Fifth Assessment Report Climate Change 2013:
584 The Physical Science Basis (Final Draft Underlying Scientific-Technical Assessment).
- 585 Jager, A., Vaclav, V., Gernert, J., Span, R., Hruby, J., 2013. Phase equilibria with hydrate formation in
586 H₂O+CO₂ mixtures modeled with reference equations of state. *Fluid Phase Equilib.* 338, 100–
587 113. doi:10.1016/j.fluid.2012.10.017
- 588 Jenkins, C., Chadwick, A., Hovorka, S.D., 2015. The state of the art in monitoring and verification —
589 Ten years on. *Int. J. Greenh. Gas Control* 40, 312–349. doi:10.1016/j.ijggc.2015.05.009
- 590 Kim, Y., Wan, J., Kneafsey, T.J., Tokunaga, T.K., 2012. Dewetting of silica surfaces upon reactions with
591 supercritical CO₂ and brine: Pore-scale studies in micromodels. *Environ. Sci. Technol.* 46, 4228–
592 4235. doi:10.1021/es204096w
- 593 Krukowski, E.G., Goodman, A., Rother, G., Ilton, E.S., Guthrie, G., Bodnar, R.J., 2015. FT-IR study of
594 CO₂ interaction with Na⁺ exchanged montmorillonite. *Appl. Clay Sci.* 114, 61–68.
595 doi:10.1016/j.clay.2015.05.005
- 596 Loring, J.S., Chen, J., Bénézeth, P., Qafoku, O., Ilton, E.S., Washton, N.M., Thompson, C.J., Martin,
597 P.F., McGrail, B.P., Rosso, K.M., Felmy, A.R., Schaef, H.T., 2015. Evidence for Carbonate Surface
598 Complexation during Forsterite Carbonation in Wet Supercritical Carbon Dioxide. *Langmuir* 31,
599 7533–7543. doi:10.1021/acs.langmuir.5b01052
- 600 Loring, J.S., Ilton, E.S., Thompson, C.J., Martin, P.F., Rosso, K.M., Felmy, A.R., Schaef, H.T., 2014. In
601 Situ Study of CO₂ and H₂O Partitioning between Na – Montmorillonite and Variably Wet
602 Supercritical Carbon Dioxide. *Langmuir* 30, 6120–6128.
- 603 Loring, J.S., Schaef, H.T., Turcu, R.V.F., Thompson, C.J., Miller, Q.R.S., Martin, P.F., Hu, J., Hoyt, D.W.,
604 Qafoku, O., Ilton, E.S., Felmy, A.R., Rosso, K.M., 2012a. In situ molecular spectroscopic evidence
605 for CO₂ intercalation into montmorillonite in supercritical carbon dioxide. *Langmuir* 28, 7125–8.
606 doi:10.1021/la301136w
- 607 Loring, J.S., Thompson, C.J., Wang, Z., Joly, A.G., Sklarew, D.S., Schaef, H.T., Ilton, E.S., Rosso, K.M.,
608 Felmy, A.R., 2011. In situ infrared spectroscopic study of forsterite carbonation in wet
609 supercritical CO₂. *Environ. Sci. Technol.* 45, 6204 – 6210. doi:10.1021/es201284e
- 610 Loring, J.S., Thompson, C.J., Zhang, C., Wang, Z., Schaef, H.T., Rosso, K.M., 2012b. In situ infrared
611 spectroscopic study of brucite carbonation in dry to water-saturated supercritical carbon
612 dioxide. *J. Phys. Chem. A* 116, 4768–77. doi:10.1021/jp210020t
- 613 McCool, B., Tripp, C.P., 2005. Inaccessible hydroxyl groups on silica are accessible in supercritical
614 CO₂. *J. Phys. Chem. B* 109, 8914–8919. doi:10.1021/jp050192q
- 615 McGrail, B.P., Schaef, H.T., Glezakou, V. -a., Dang, L.X., Owen, A.T., 2009. Water reactivity in the
616 liquid and supercritical CO₂ phase: Has half the story been neglected? *Energy Procedia* 1, 3415–
617 3419. doi:10.1016/j.egypro.2009.02.131
- 618 Miller, Q.R.S., Thompson, C.J., Loring, J.S., Windisch, C.F., Bowden, M.E., Hoyt, D.W., Hu, J.Z., Arey,
619 B.W., Rosso, K.M., Schaef, H.T., 2013. Insights into silicate carbonation processes in water-
620 bearing supercritical CO₂ fluids. *Int. J. Greenh. Gas Control* 15, 104–118.
621 doi:10.1016/j.ijggc.2013.02.005

- 622 Murphy, R., Lammers, K., Smirnov, A., Schoonen, M. a. a., Strongin, D.R., 2011. Hematite reactivity
623 with supercritical CO₂ and aqueous sulfide. *Chem. Geol.* 283, 210–217.
624 doi:10.1016/j.chemgeo.2011.01.018
- 625 Murphy, R., Lammers, K., Smirnov, A., Schoonen, M. a. a., Strongin, D.R., 2010. Ferrihydrite phase
626 transformation in the presence of aqueous sulfide and supercritical CO₂. *Chem. Geol.* 271, 26–
627 30. doi:10.1016/j.chemgeo.2009.12.008
- 628 Nakamoto, K., Fujita, J., Tanaka, S., Kobayashi, M., 1957. Infrared Spectra of Metallic Complexes. IV.
629 Comparison of the Infrared Spectra of Unidentate and Bidentate Metallic Complexes. *J. Am.*
630 *Chem. Soc.* 79, 4904 – 4908.
- 631 Oparin, R., Tassaing, T., Danten, Y., Besnard, M., 2005. Water-carbon dioxide mixtures at high
632 temperatures and pressures: local order in the water rich phase investigated by vibrational
633 spectroscopy. *J. Chem. Phys.* 123, 224501. doi:10.1063/1.2131052
- 634 Oparin, R., Tassaing, T., Danten, Y., Besnard, M., 2004. A vibrational spectroscopic study of structure
635 evolution of water dissolved in supercritical carbon dioxide under isobaric heating. *J. Chem.*
636 *Phys.* 120, 10691–8. doi:10.1063/1.1739214
- 637 Pauwels, H., Gaus, I., le Nindre, Y.M., Pearce, J., Czernichowski-Lauriol, I., 2007. Chemistry of fluids
638 from a natural analogue for a geological CO₂ storage site (Montmiral, France): Lessons for CO₂-
639 water-rock interaction assessment and monitoring. *Appl. Geochemistry* 22, 2817–2833.
640 doi:10.1016/j.apgeochem.2007.06.020
- 641 Plettinger, S., Chou, L., Wollast, R., 1994. Kinetics and Mechanisms of Dissolution of Silica at Room
642 Temperature and Pressure. *Mineral. Mag.* 58A, 728–729. doi:10.1180/minmag.1994.58A.2.116
- 643 Pruess, K., Müller, N., 2009. Formation dry-out from CO₂ injection into saline aquifers: 1. Effects of
644 solids precipitation and their mitigation. *Water Resour. Res.* 45, n/a–n/a.
645 doi:10.1029/2008WR007101
- 646 Rimstidt, J.D., 2015. Rate equations for sodium catalyzed quartz dissolution. *Geochim. Cosmochim.*
647 *Acta* 167, 195–204. doi:10.1016/j.gca.2015.07.030
- 648 Sanna, A., Uibu, M., Caramanna, G., Kuusik, R., Maroto-Valer, M.M., 2014. A review of mineral
649 carbonation technologies to sequester CO₂. *Chem. Soc. Rev.* doi:10.1039/c4cs00035h
- 650 Schaefer, H.T., Loring, J.S., Glezakou, V.A., Miller, Q.R.S., Chen, J., Owen, A.T., Lee, M.S., Ilton, E.S.,
651 Felmy, A.R., McGrail, B.P., Thompson, C.J., 2015. Competitive sorption of CO₂ and H₂O in 2:1
652 layer phyllosilicates. *Geochim. Cosmochim. Acta* 161, 248–257. doi:10.1016/j.gca.2015.03.027
- 653 Schwarz, J., Driscoll, C., Bhanot, a. ., 1984. The zero point of charge of silica—alumina oxide
654 suspensions. *J. Colloid Interface Sci.* 97, 55–61. doi:10.1016/0021-9797(84)90274-1
- 655 Smit, W., Holten, C.L.M., Stein, H.N., 1978. A Radiotracer Determination of the Adsorption of Sodium
656 Ion in the Compact Part of the Double Layer of Vitreous Silica. *J. Electroanal. Chem. Interfacial*
657 *Electrochem.* 91, 393–394. doi:10.1016/S0022-0728(78)80290-3

- 658 Span, R., Wagner, W., 1996. A New Equation of State for Carbon Dioxide Covering the Fluid Region
659 from the Triple-Point Temperature to 1100 K at Pressures up to 800 MPa. *J. Phys. Chem. Ref.*
660 *Data* 25, 1509. doi:10.1063/1.555991
- 661 Spycher, N., Pruess, K., Ennis-King, J., 2003. CO₂-H₂O mixtures in the geological sequestration of CO₂.
662 I. Assessment and calculation of mutual solubilities from 12 to 100°C and up to 600 bar.
663 *Geochim. Cosmochim. Acta* 67, 3015–3031. doi:10.1016/S0016-7037(03)00273-4
- 664 Thompson, C.J., Loring, J.S., Rosso, K.M., Wang, Z., 2013. Comparative reactivity study of forsterite
665 and antigorite in wet supercritical CO₂ by in situ infrared spectroscopy. *Int. J. Greenh. Gas*
666 *Control* 18, 246 – 255. doi:10.1016/j.ijggc.2013.07.007
- 667 Thompson, C.J., Martin, P.F., Chen, J., Benezeth, P., Schaefer, H.T., Rosso, K.M., Felmy, A.R., Loring, J.S.,
668 2014. Automated high-pressure titration system with in situ infrared spectroscopic detection.
669 *Rev. Sci. Instrum.* 85, 044102. doi:10.1063/1.4870411
- 670 Tripp, C.P., Combes, J.R., 1998. Chemical Modification of Metal Oxide Surfaces in Supercritical CO₂:
671 The Interaction of Supercritical CO₂ with the Adsorbed Water Layer and the Surface Hydroxyl
672 Groups of a Silica Surface. *Langmuir* 14, 7348–7352. doi:10.1021/la9805701
- 673 Wan, J., Kim, Y., Tokunaga, T.K., 2014. Contact angle measurement ambiguity in supercritical CO₂–
674 water–mineral systems: Mica as an example. *Int. J. Greenh. Gas Control* 31, 128–137.
675 doi:10.1016/j.ijggc.2014.09.029
- 676 Wang, Z., Felmy, A.R., Thompson, C.J., Loring, J.S., Joly, A.G., Rosso, K.M., Schaefer, H.T., Dixon, D. a.,
677 2013. Near-infrared spectroscopic investigation of water in supercritical CO₂ and the effect of
678 CaCl₂. *Fluid Phase Equilib.* 338, 155 – 163. doi:10.1016/j.fluid.2012.11.012
- 679 Wigley, M., Dubacq, B., Kampman, N., Bickle, M., 2013. Controls of sluggish, CO₂-promoted,
680 hematite and K-feldspar dissolution kinetics in sandstones. *Earth Planet. Sci. Lett.* 362, 76–87.
681 doi:10.1016/j.epsl.2012.11.045
- 682 Wijnen, P.W.J.G., Beelen, T.P.M., De Haan, J.W., Van De Ven, L.J.M., Van Santen, R.A., 1990. The
683 Structure Directing Effect of Cations in Aqueous Silicate Solutions. A ²⁹ Si-NMR Study. *Colloids*
684 *and Surfaces* 45, 255 – 268.
- 685 Xu, T., Apps, J. a., Pruess, K., 2004. Numerical simulation of CO₂ disposal by mineral trapping in deep
686 aquifers. *Appl. Geochemistry* 19, 917–936. doi:10.1016/j.apgeochem.2003.11.003
- 687 Yagi, Y., Tsugane, H., Inomata, H., Saito, S., 1993. Density dependence of fermi resonance of
688 supercritical carbon dioxide. *J. Supercrit. Fluids* 6, 139–142. doi:10.1016/0896-8446(93)90012-
689 M
- 690 Yang, Q., Matter, J., Stute, M., Takahashi, T., O’Mullan, G., Umemoto, K., Clauson, K., Dueker, M.E.,
691 Zakharova, N., Goddard, J., Goldberg, D., 2014. Groundwater hydrogeochemistry in injection
692 experiments simulating CO₂ leakage from geological storage reservoir. *Int. J. Greenh. Gas*
693 *Control* 26, 193–203. doi:10.1016/j.ijggc.2014.04.025
- 694 Zhang, M., Bachu, S., 2011. Review of integrity of existing wells in relation to CO₂ geological storage:
695 What do we know? *Int. J. Greenh. Gas Control* 5, 826–840. doi:10.1016/j.ijggc.2010.11.006

- 696 Zhuravlev, L.T., 2000. The surface chemistry of amorphous silica . Zhuravlev model. Colloids Surfaces
697 A Physicochem. Eng. Asp. 173, 1–38.
- 698 Zhuravlev, L.T., 1993. Surface Characterization of Amorphous Silica - a Review of Work from the
699 Former Ussr. Colloids Surfaces a-Physicochemical Eng. Asp. 74, 71–90.
- 700 Zhuravlev, L.T., 1989. Structurally bound water and surface characterization of amorphous silica.
701 Pure Appl. Chem. 61, 1969–1976. doi:10.1351/pac198961111969
- 702